



**Non-Hermitian skin effect in periodically driven dissipative ultracold atoms**Zhao-Fan Cai <sup>1</sup>, Tao Liu <sup>1,\*</sup>, and Zhongmin Yang<sup>1,2,3,†</sup><sup>1</sup>*School of Physics and Optoelectronics, South China University of Technology, Guangzhou 510640, China*<sup>2</sup>*Research Institute of Future Technology, South China Normal University, Guangzhou 510006, China*<sup>3</sup>*State Key Laboratory of Luminescent Materials and Devices and Institute of Optical Communication Materials, South China University of Technology, Guangzhou 510640, China*

(Received 11 November 2023; revised 7 May 2024; accepted 5 June 2024; published 25 June 2024)

The non-Hermitian skin effect (NHSE), characterized by the collapse of bulk-band eigenstates into the localized boundary modes of the systems, is one of most striking properties in the field of non-Hermitian physics. Unique physical phenomena related to the NHSE have attracted a great deal of interest; however, their experimental realization usually requires nonreciprocal hopping, which faces a great challenge in ultracold-atom systems. In this work we propose the realization of the NHSE in a one-dimensional optical lattice by periodically driven ultracold atoms in the presence of staggered atomic loss. By studying the effective Floquet Hamiltonian in the high-frequency approximation, we reveal the underlying mechanism for the periodic-driving-induced NHSE. We find that the robust NHSE can be tuned by the driving phase, which is manifested by the dynamical localization. Most remarkably, we uncover the periodic-driving-induced critical skin effect for two coupled chains with different driving phases, accompanied by the appearance of size-dependent topological in-gap modes. Our study provides a feasible way to observe the NHSE and explore the corresponding unique physical phenomena due to the interplay of non-Hermiticity and many-body statistics in ultracold-atom systems.

DOI: [10.1103/PhysRevA.109.063329](https://doi.org/10.1103/PhysRevA.109.063329)**I. INTRODUCTION**

Non-Hermitian systems exhibit many unique physical phenomena without Hermitian counterparts, which have drawn extensive research interest in recent years [1–43]. In particular, one of their striking physical properties is the emergence of the non-Hermitian skin effect (NHSE) [7–12,26–31]. By the NHSE, an extensive number of bulk modes collapse into localized boundary modes within the open boundaries. The NHSE has its intrinsic topological origin associated with the point gap [23,30] and it can lead to many exotic physical phenomena, e.g., the breakdown of conventional Bloch band theory [7–9], nonunitary scaling of non-Hermitian localization [44], and entanglement phase transitions [39].

Although several theoretical proposals have been devoted to exploring the NHSEs and several related novel physical phenomena [34,43,45], experimental studies have largely remained behind. The main obstacle, in most cases, is the challenging requirement of the nonreciprocal hopping in achieving the NHSE for many experimental platforms. At present, most experiments are limited to classical phononic and optical structures [46–48] and electrical circuits [49,50]. A more operational approach is to utilize on-site gain and loss or equivalently imbalanced on-site dissipation [31,35,38,51,52].

Ultracold quantum gases in optical lattices provide a promising platform for studying intriguing quantum physics due to their high controllability, rich lattice structures, and

many-body nature [53–56], which have been widely utilized to explore topological phases [54,55] and many-body physics [56]. Furthermore, NHSEs have been theoretically proposed [51,57,58] and also experimentally observed [38,52] in optical lattices of ultracold atoms. These studies usually rely on complicated lattice structures to achieve the NHSE assisted by atomic loss.

Alternatively, we may realize the NHSE and study the associated physical phenomena in an experimentally accessible optical lattice of ultracold atoms based on Floquet engineering. Floquet engineering is a versatile tool that tailors a system using the periodic driving and has produced a wide variety of fascinating physics in the field of ultracold atoms due to their excellent dynamic control [59–63]. Most recently, loss-induced NHSEs have been reported in a periodically driven photonic structure [64] and acoustic metamaterial [65]. Both proposals are classical settings, and it is natural to achieve the NHSE in periodically driven ultracold-atom systems, which would offer an exciting opportunity for studying the NHSE and its interplay with many-body interaction.

In this paper we theoretically propose to realize the NHSE in periodically driven dissipative ultracold atoms. By periodically driving the one-dimensional (1D) optical lattice of ultracold atoms in the presence of staggered atomic loss, we observe the NHSE with all the modes localized at boundaries, which can be manifested by dynamical localization. The direction of the skin-mode localization can be controlled by the driving phase and characterized by the winding number. Moreover, by coupling two periodically driven chains with different driving phases, we study the critical skin effect, with the appearance of size-dependent topological in-gap modes.

\*Contact author: [liutao0716@scut.edu.cn](mailto:liutao0716@scut.edu.cn)†Contact author: [yangzm@scut.edu.cn](mailto:yangzm@scut.edu.cn)

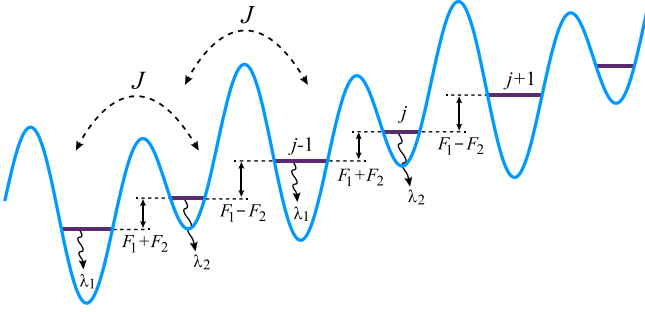


FIG. 1. Schematic showing the tilted optical lattice of ultracold atoms with periodic modulation of on-site potential. The bare atomic tunnel coupling is represented by  $J$ ;  $\lambda_1$  and  $\lambda_2$ , with  $\lambda_2 = \lambda_1 + \lambda$ , denote the staggered atomic losses at odd and even sites, respectively; and on-site potential modulations are expressed as  $F_1 = F \cos(\omega t + \phi)$  and  $F_2 = F \sin(\omega t)$ .

The rest of this paper is organized as follows. In Secs. II A and II B we present a 1D optical lattice constructed by dissipative ultracold atoms under the periodic modulation of on-site potential. When the staggered atomic loss is introduced along the chain, we observe the NHSE. We discuss the effect of disorder and dynamical localization in Secs. II C and II D, respectively. To further demonstrate the novel non-Hermitian physics in periodically driven system, we study the critical skin effect in Sec. III. We summarize the key findings in Sec. IV.

## II. PERIODICALLY DRIVEN DISSIPATIVE ULTRACOLD ATOMS

### A. Model and Floquet Hamiltonian

To induce the NHSE, we consider periodically driven dissipative quantum systems, which can be experimentally realized by using well-developed techniques of Floquet engineering in ultracold atoms, including the approaches of lattice shaking, laser-assisted tunneling, modulation of external field gradients, and a combination of these methods [59–63]. In 1D dissipative ultracold atoms, by periodic modulation of on-site potential in 1D optical lattices in a tilted optical lattice (see Fig. 1), we construct the periodically driven Hamiltonian  $\mathcal{H}_p(t) = \mathcal{H}_0 + \mathcal{H}_d(t)$ , with

$$\mathcal{H}_0 = -J \sum_{j=1}^{L-1} (c_{j+1}^\dagger c_j + \text{H.c.}) - i\lambda \sum_{j=1}^{L/2} n_{2j} - i\lambda_1 \sum_{j=1}^L n_j, \quad (1)$$

$$\mathcal{H}_d(t) = \sum_{j=1}^L F \left( \cos(\omega t + \phi) j + \sin(\omega t) \frac{3 + (-1)^j}{2} \right) n_j. \quad (2)$$

Here  $\mathcal{H}_0$  is the undriven Hamiltonian in the presence of staggered dissipation, with  $\lambda_1$  and  $\lambda_2 = \lambda_1 + \lambda$  the atomic loss rates at odd and even sites, respectively (see Fig. 1), and  $\mathcal{H}_d$  represents periodically modulated on-site potential in a tilted optical lattice, with its first term being on-site energy offset along the lattice and its second term being staggered on-site potential. In addition,  $c_j^\dagger$  is the creation operator at the  $j$ th lattice site;  $n_j = c_j^\dagger c_j$  is the corresponding density operator;

$F$ ,  $\omega$ , and  $\phi$  are the driving strength, frequency, and phase, respectively; and  $J$  is the atomic hopping rate. The details of experimental proposals are shown in Appendix A. Without loss of generality, we set  $\lambda_1 = 0$  below.

By performing a unitary transformation  $\mathcal{U}(t) = \exp[i \int^t \mathcal{H}_d(t') dt']$  to a rotating frame of reference (see Appendix B),  $\mathcal{H}_p$  is rewritten as

$$\mathcal{H}(t) = \sum_j [(uc_{2j}^\dagger c_{2j-1} + vc_{2j+1}^\dagger c_{2j} + \text{H.c.}) - i\lambda n_{2j}], \quad (3)$$

where

$$u = -J e^{i\sqrt{2}\alpha \cos(\phi/2 + \pi/4) \sin(\omega t + \phi/2 - \pi/4)}, \quad (4)$$

$$v = -J e^{i\sqrt{2}\alpha \sin(\phi/2 + \pi/4) \cos(\omega t + \phi/2 - \pi/4)}, \quad (5)$$

with  $\alpha = \sqrt{2}F/\omega$ . According to the Floquet theorem [66], a time-periodic Hamiltonian  $\mathcal{H}(t) = \mathcal{H}(t + T)$ , with the driving period  $T = 2\pi/\omega$ , is governed by the Schrödinger equation  $i\partial_t |\psi_n(t)\rangle = \mathcal{H}(t) |\psi_n(t)\rangle$ . There exists a complete set of orthogonal solutions  $|\psi_n(t)\rangle = e^{-iE_n t} |u_n(t)\rangle$ , with  $|u_n(t)\rangle = |u_n(t + T)\rangle$  and quasienergy  $E_n$ . In this work we are interested in the stroboscopic dynamics governed by the time-independent effective Floquet Hamiltonian  $\mathcal{H}_F$ , defined as

$$U(T) = \mathcal{T} \exp \left( -i \int_0^T \mathcal{H}(t') dt' \right) = e^{-i\mathcal{H}_F T}, \quad (6)$$

where  $\mathcal{T}$  is the time-ordering operator and  $U(T) |\psi_n(0)\rangle = e^{-iE_n T} |\psi_n(0)\rangle$ . Due to the non-Hermiticity of  $\mathcal{H}(t)$ , the Floquet operator  $U(T)$  is not unitary and the quasienergy  $E_n$  can be complex.

### B. Non-Hermitian skin effect

To reveal the periodically driven skin effect for the dissipative ultracold-atom system proposed above, we plot the complex quasienergy spectrum  $E_n$  and corresponding density distributions  $|\psi_n|^2$  of the Floquet Hamiltonian  $\mathcal{H}_F$ , as shown in Fig. 2. The quasienergies are calculated under both periodic boundary conditions (PBCs) and open boundary conditions (OBCs), while density distributions are under OBCs. The complex quasienergy spectrum of the pure dissipative system with  $\alpha = 0$  is insensitive to the boundary conditions and there exists no NHSE [see Fig. 2(a)]. In addition, the only periodically driven ultracold atoms with  $\lambda = 0$  cannot induce the NHSE [see Fig. 2(b)].

For the periodically driven and dissipative ultracold-atom chain in the presence of the staggered loss, i.e.,  $\alpha \neq 0$  and  $\lambda \neq 0$ , the complex quasienergy spectrum is sensitive to boundary conditions [see Figs. 2(c i), 2(d i), and 2(e i)]. The periodic drive induces the formation of point gaps, a loop in the complex plane [see red dots in Figs. 2(c i), 2(d i), and 2(e i)], encircling the open-arc spectrum of OBCs (blue dots). Figures 2(c ii), 2(d ii), and 2(e ii) plot the density distributions  $|\psi_n|^2$  of all the Floquet eigenmodes, where all the modes are localized at the boundaries. Moreover, these non-Hermitian skin modes can be localized at either right [see Figs. 2(c ii) and 2(d ii)] or left [see Fig. 2(e ii)] boundaries, determined by the driving phase  $\phi$ . Therefore, our periodic-modulation approach

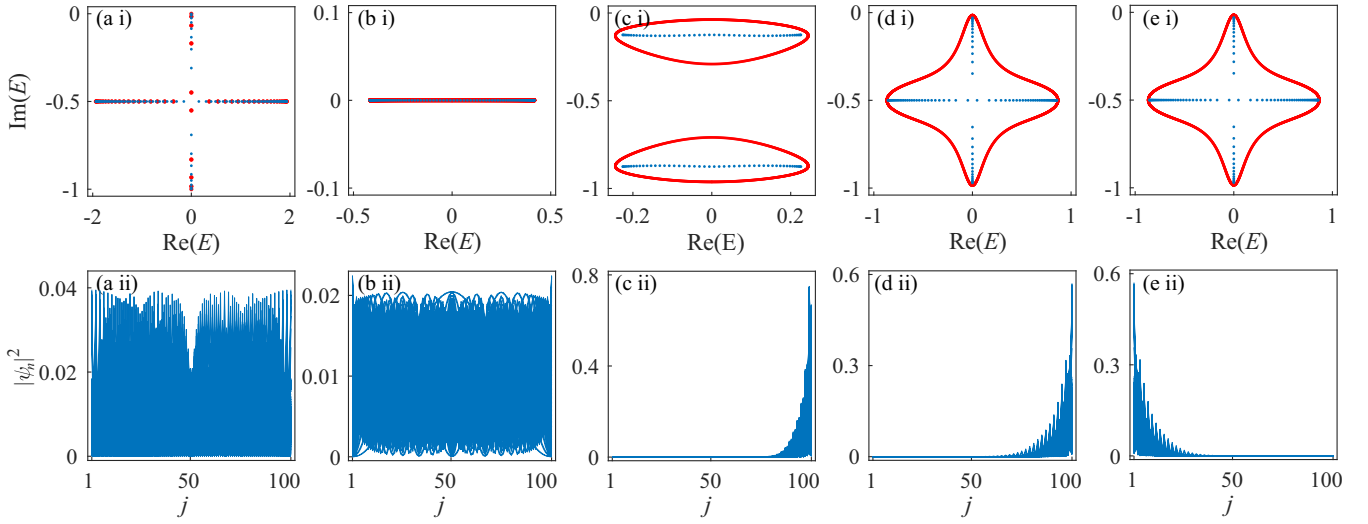


FIG. 2. Complex quasienergy spectrum  $E_n$  and corresponding density distributions  $|\psi_n|^2$  of the Floquet Hamiltonian  $\mathcal{H}_F$ . The red and blue dots indicate the quasienergies under PBCs and OBCs, respectively. (a) Pure dissipative ultracold atoms with  $\alpha = 0$ . (b) The only periodic drive with  $\alpha = 2$ ,  $\omega = 2\pi$ , and  $\lambda = 0$ . Also shown are the periodically driven dissipative ultracold atoms with (c)  $\alpha = 2$ ,  $\omega = 2\pi$ , and  $\phi = 0$ ; (d)  $\alpha = 1.5$ ,  $\omega = 3\pi$ , and  $\phi = 0$ ; and (e)  $\alpha = 1.5$ ,  $\omega = 3\pi$ , and  $\phi = \pi$ . The other parameters are  $\lambda/J = 1.0$  and  $L = 100$ .

realizes a tunable 1D NHSE in the dissipative ultracold-atom system.

The NHSE has its topological origin, which is characterized by the point-gap topology with the topological invariant of the winding number [30]

$$\mathcal{W}(E_r) = \int_{-\pi}^{\pi} \frac{dk}{2\pi i} \partial_k \ln \det[\mathcal{H}_F(k) - E_r], \quad (7)$$

where  $\mathcal{H}_F(k)$  is the Floquet Hamiltonian in momentum space and  $E_r$  is a reference energy point inside the loop of the point gap. The  $\mathcal{W}(E_r)$  counts the number of times that the complex spectrum of  $\mathcal{H}_F(k)$  encircles  $E_r$ .

We analytically calculate  $\mathcal{W}(E_r)$  by approximating  $\mathcal{H}_F(k)$  using the time-independent effective Hamiltonian  $\mathcal{H}_{\text{eff}}(k)$ , obtained by the Floquet-Magnus expansion in the high-frequency approximation [67–69]. For  $\omega \gg J, F$ , the effective Hamiltonian  $\mathcal{H}_{\text{eff}}(k)$  (see details in Appendix C) is derived as

$$\begin{aligned} \mathcal{H}_{\text{eff}}(k) = & - \sum_k [JJ_0(\alpha)(1 + e^{-ik})c_{k,A}^\dagger c_{k,B} + \text{H.c.}] \\ & - s \frac{2J^2 J_{-1}^2(\alpha)}{\omega} \sum_k \sin(k)(c_{k,A}^\dagger c_{k,A} - c_{k,B}^\dagger c_{k,B}) \\ & - i\lambda \sum_k c_{k,B}^\dagger c_{k,B}, \end{aligned} \quad (8)$$

where  $A$  and  $B$  denote two sublattice sites in the unit cell due to the staggered loss,  $J_m(\alpha)$  is the Bessel function of the first kind, and  $s = 1$  ( $-1$ ), corresponding to  $\phi = 0$  ( $\pi$ ), the winding number is calculated as  $\mathcal{W} = -1$  ( $\mathcal{W} = 1$ ) for  $\phi = 0$  ( $\pi$ ).

To further elucidate the mechanism of the Floquet-induced NHSE considered here, we write the real-space effective Hamiltonian in the high-frequency expansion (see details in

Appendix C) as

$$\begin{aligned} \mathcal{H}_{\text{eff}} = & - \sum_j [JJ_0(\alpha)c_{2j}^\dagger c_{2j-1} + JJ_0(\alpha)c_{2j+1}^\dagger c_{2j} + \text{H.c.}] \\ & - \sum_j \left( is \frac{2J^2 J_{-1}^2(\alpha)}{\omega} c_{2j+1}^\dagger c_{2j-1} + \text{H.c.} \right) \\ & + \sum_j \left( is \frac{2J^2 J_{-1}^2(\alpha)}{\omega} c_{2j+2}^\dagger c_{2j} + \text{H.c.} \right) - i\lambda \sum_j c_{2j}^\dagger c_{2j}. \end{aligned} \quad (9)$$

The Hamiltonian  $\mathcal{H}_{\text{eff}}$  in Eq. (9) describes an effective 1D lattice in the presence of both nearest-neighbor and next-nearest-neighbor hoppings, forming a zigzag lattice (see Fig. 3). Moreover, a  $\pi/2$  magnetic flux threads through each triangular plaquette in the clockwise and counterclockwise

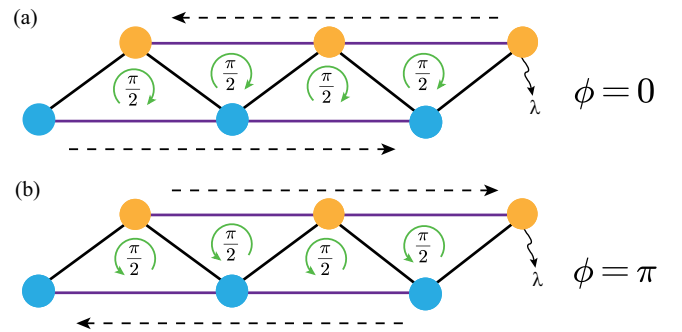


FIG. 3. Schematic showing the 1D zigzag lattice described by Eq. (9). The even sites (yellow circles) are dissipated by  $\lambda = \lambda_2 - \lambda_1$ . A  $\pi/2$  magnetic flux threads through each triangular plaquette in the clockwise and counterclockwise directions for (a)  $\phi = 0$  and (b)  $\phi = \pi$  due to the complex next-nearest-neighbor hopping in Eq. (9). Such a nonzero flux leads to opposite particle transport along the odd and even lattice sites, indicated by the dashed arrows.

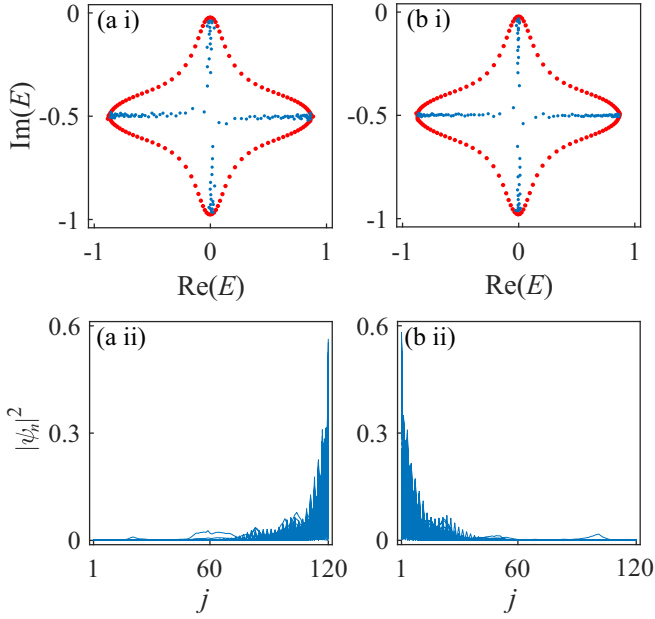


FIG. 4. Complex quasienergy spectrum  $E_n$  and corresponding density distributions  $|\psi_n|^2$  of the Floquet Hamiltonian  $\mathcal{H}_F$  in the presence of on-site disordered potential  $\mathcal{H}_{\text{dis}}$  for (a)  $\phi = 0$  and (b)  $\phi = \pi$ . The red and blue dots indicate the quasienergies under PBCs and OBCs, respectively. The other parameters are  $\alpha = 1.5$ ,  $\omega = 3\pi$ ,  $\lambda/J = 1$ ,  $W/J = 5$ , and  $L = 120$ .

directions for  $\phi = 0$  and  $\phi = \pi$  due to the complex next-nearest-neighbor hopping in Eq. (9). Such a nonzero flux leads to opposite particle transports along the odd and even lattice sites [35,70,71]. Due to the larger loss for the even sites, the particle transport along the odd sites are favored and the backflow on even sites is suppressed. This leads to skin modes at the right and left boundaries for  $\phi = 0$  and  $\phi = \pi$ , respectively.

### C. Robustness against disorder

The intrinsic topological nature of the NHSE in periodically driven dissipative ultracold-atom system indicates its robust against local disorders. Here we consider the introduction of the on-site disordered potential into the periodically driven dissipative system with the system Hamiltonian reading

$$\mathcal{H}_{\text{tot}}(t) = \mathcal{H}(t) + \mathcal{H}_{\text{dis}} = \mathcal{H}(t) + \sum_{j=1}^L U_j n_j, \quad (10)$$

where  $U_j$  denotes the on-site random potential, uniformly sampled in  $\in [-W/2, W/2]$ , with  $W$  denoting the disorder strength.

Figure 4 shows the complex quasienergy spectra under OBCs and PBCs and the corresponding density distributions of the Floquet Hamiltonian  $\mathcal{H}_F$  in the presence of the on-site random potential with the disorder strength  $W = 5$  for  $\phi = 0$  and  $\phi = \pi$ . The PBC eigenenergies still form a point gap, encircling all the OBC eigenvalues. All the eigenstates are localized at the right (left) boundary for  $\phi = 0$  ( $\phi = \pi$ ).

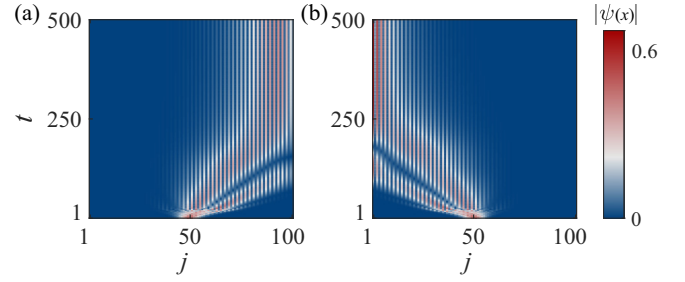


FIG. 5. Dynamical localization of the periodically driven dissipative system with (a)  $\phi = 0$  and (b)  $\phi = \pi$ . The initial states are the Gaussian wave packet  $|\psi_0\rangle = [\psi_0(1), \psi_0(2), \dots, \psi_0(L)]^T$ , with  $\psi_0(j) = \exp[-(j - j_0)^2/2\sigma^2]/\mathcal{N}$  centered at the site  $j_0 = L/2$ . Here we choose the width of the wave packet  $\sigma = 5$ . The wave packets at every time have been renormalized. The other parameters are  $\alpha = 1.5$ ,  $\omega = 3\pi$ ,  $\lambda/J = 1$ , and  $L = 100$ .

Therefore, the NHSEs remain in spite of strong disorder due to the intrinsic non-Hermitian topology of the periodically driven dissipative ultracold-atom system considered here.

### D. Dynamical localization

The NHSE can be manifested by studying the dynamical evolution. We consider the initial states as the Gaussian wave packet  $|\psi_0\rangle = [\psi_0(1), \psi_0(2), \dots, \psi_0(L)]^T$ , with  $\psi_0(j) = \exp[-(j - j_0)^2/2\sigma^2]/\mathcal{N}$  centered at the site  $j_0 = L/2$ , where  $\mathcal{N}$  is the normalization constant and  $\sigma$  denotes the width of the wave packet. The wave function at time  $t$  can be obtained by numerically calculating  $|\psi(t)\rangle = \mathcal{T} \exp[-i \int_0^t \mathcal{H}(\tau) d\tau] |\psi_0\rangle$ .

We calculate the time-dependent density distributions of the periodically driven dissipative ultracold-atom system for  $\phi = 0$  and  $\phi = \pi$ , as shown in Fig. 5. Due to the nonreciprocal nature of the considered system, as analyzed above, the wave packet is finally localized towards the right and left boundaries for  $\phi = 0$  and  $\phi = \pi$ , respectively.

## III. FLOQUET-INDUCED CRITICAL NON-HERMITIAN SKIN EFFECT

The NHSE can induce a novel critical behavior without its Hermitian counterpart, dubbed the critical NHSE [26]. More specifically, when two non-Hermitian systems with different skin lengths are coupled together, the energy spectrum

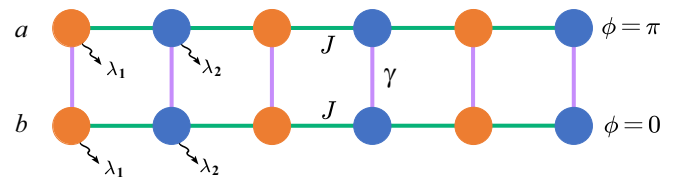


FIG. 6. Schematic showing the lattice ladder of ultracold atoms for realizing a critical NHSE. For each leg  $a$  or  $b$  of the ladder, the optical lattice has the same structure as the one in Fig. 1, which is periodically modulated and staggered with alternating losses  $\lambda_1$  and  $\lambda_2$ , with  $\lambda = \lambda_2 - \lambda_1$ . Along the rung, driving phases are set as  $\phi = 0$  and  $\phi = \pi$ , respectively;  $\gamma$  is the hopping strength along the rung.

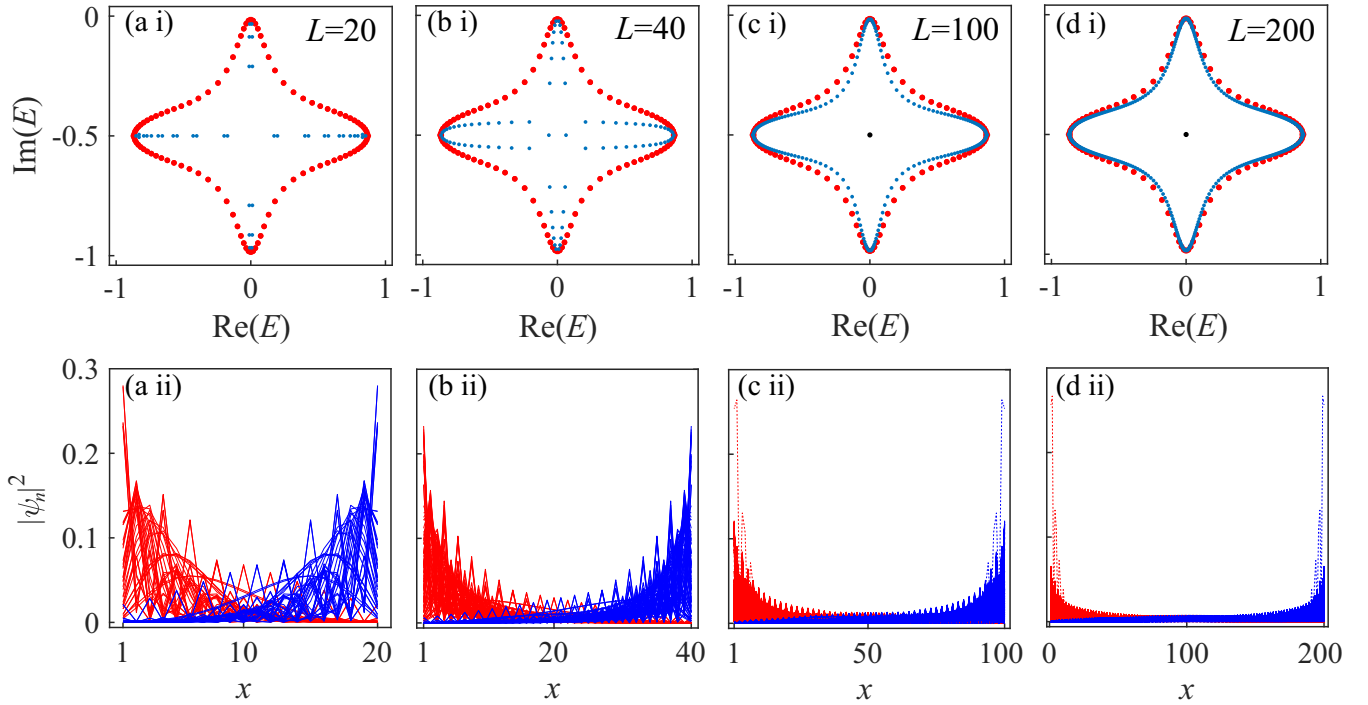


FIG. 7. Complex quasienergy spectrum  $E_n$  and corresponding density distributions  $|\psi_n|^2$  of the Floquet Hamiltonian  $\mathcal{H}_L^F$  of the driving ladder for different sizes from  $L = 20$  to  $200$ . The red and blue dots indicate the quasienergies under PBCs and OBCs, respectively. The red and blue lines represent the density distributions  $|\psi_n|^2$  of legs  $a$  and  $b$ , respectively. (c i) and (d i) As the size  $L$  increases, the topological in-gap degenerate states (black dots) with zero real parts of complex eigenenergies appear. (c ii) and (d ii) The corresponding state distributions are shown in with dashed curves. The parameters are  $\alpha = 1.5$ ,  $\omega = 3\pi$ ,  $\lambda/J = 1.0$ , and  $\gamma/J = 0.005$ .

discontinuously jumps across a critical point in the thermodynamic limit. The critical skin effects have been studied in static systems [26,27,72,73]. Here we show that such a critical behavior can also be observed in the driving system.

To study the Floquet-induced critical NHSE, we consider the quasi-one-dimensional ladder of ultracold atoms, as

shown in Fig. 6. For each leg  $a$  or  $b$  of the ladder, the optical lattice has the same structure as the one in Fig. 1, which is periodically modulated and staggered with alternating losses  $\lambda_1$  and  $\lambda_2$ . Along the rung, driving phases are set as  $\phi = 0$  and  $\phi = \pi$ , respectively. The Hamiltonian of the driving ladder is written in the rotating frame of reference (see Appendix B) as

$$\begin{aligned} \mathcal{H}_L(t) = & - \sum_{j=1}^{L/2} (J_-^* a_{2j}^\dagger a_{2j-1} + J_+^* b_{2j}^\dagger b_{2j-1} + \text{H.c.}) - \sum_{j=1}^{L/2-1} (J_+ a_{2j+1}^\dagger a_{2j} + J_- b_{2j+1}^\dagger b_{2j} + \text{H.c.}) - \sum_{j=1}^{L/2} i\lambda (a_{2j}^\dagger a_{2j} + b_{2j}^\dagger b_{2j}) \\ & - \sum_{j=1}^L \gamma (a_j^\dagger b_j + \text{H.c.}), \end{aligned} \quad (11)$$

where  $J_\pm = J e^{i\alpha \cos(\omega t \pm \pi/4)}$  represents the hopping strength for legs  $a$  and  $b$ ,  $\lambda$  indicates on-site dissipation with  $\lambda = \lambda_2 - \lambda_1$ , and  $\gamma$  is the hopping strength along the rung. The Floquet Hamiltonian  $\mathcal{H}_L^F$  of the ladder is defined as  $U(T) = \mathcal{T} \exp[-i \int_0^T \mathcal{H}_L(t') dt'] = e^{-i\mathcal{H}_L^F T}$ .

Figure 7 shows the complex quasienergy spectrum and corresponding density distributions of  $\mathcal{H}_L^F$  for different sizes  $L$ . The PBC spectrum (red dots) is not sensitive to the system size, while the OBC spectrum (blue dots) changes remarkably as the size  $L$  of the coupled chains increases from  $L = 20$  to  $200$  in spite of the weak-coupling strength between two chains with  $\gamma/J = 0.005$ . For the small size  $L = 20$ , the OBC spectrum of the coupled chains mostly resembles the one of

the respective single chains in Figs. 2(d i) and 2(e i). As the size  $L$  increases, the OBC spectrum changes and the bulk OBC spectrum approaches the PBC spectrum of the coupled chains at the large size  $L = 200$  [see Fig. 7(d i)]. Moreover, the energy spectrum in the large-size coupled chains under OBCs discontinuously jumps across the critical point  $\gamma/J = 0$ . Therefore, the critical skin effect occurs in the periodically driven ladder.

Mostly remarkably, the critical skin effect can be manifested by the size-dependent topological phase crossovers. For  $\gamma/J = 0$ , the system is decoupled into two topologically trivial chains, while for the nonzero coupling strength  $\gamma/J \neq 0$ , the momentum-space Hamiltonian  $H_L(k, t)$  in Eq. (11)

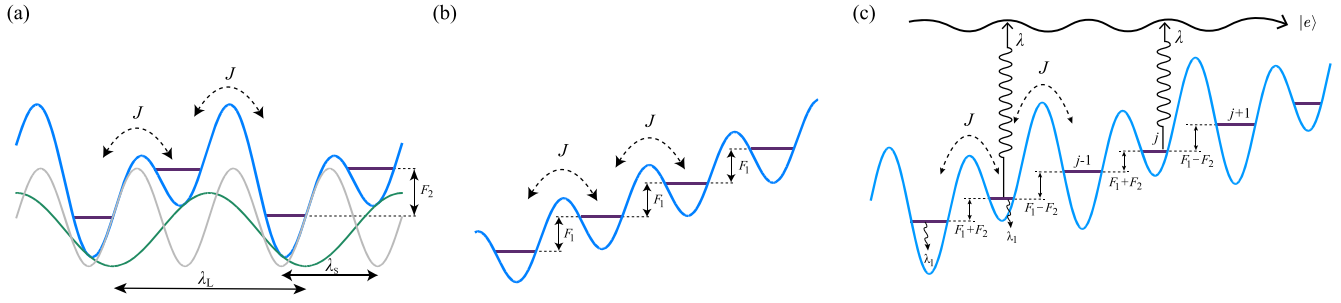


FIG. 8. Schematic showing the dynamical superlattice potential to realize the periodically driven Hamiltonian  $\mathcal{H}_p(t) = \mathcal{H}_0 + \mathcal{H}_d(t)$ . The periodically modulated potential  $\mathcal{H}_d(t)$  consists of (a) the time-dependent staggered on-site potential and (b) the time-dependent tilted on-site potential. (a) The one-dimensional dynamical optical superlattice with the time-dependent staggered on-site potential is created by superimposing a stationary lattice and a dynamical one with different periodicities. (b) An additional time-periodic modulation of the lattice position is superimposed to create the time-dependent tilted potential. (c) When the atoms are prepared in the first-band state, the staggered dissipation rates  $\lambda_1$  and  $\lambda_2 = \lambda_1 + \lambda$  at odd and even sites in  $\mathcal{H}_0$  are realized via exciting the state in the first band at even sites to the higher-level state  $|e\rangle$ , where the additional dissipation  $\lambda$  is controlled by the intensity of the external optical beam.

respects chiral symmetry, which supports topological boundary modes (see details in Appendix D). As shown in Figs. 7(a i)–7(d i), there exist no in-gap states for the small size of the ladder [see Figs. 7(a i) and 7(b i)]. However, as the size increases, topological degenerate in-gap states appear [see black dots in Figs. 7(c i) and 7(d i)]. These in-gap states are localized at the system’s boundaries [see Figs. 7(c ii) and 7(d ii)]. In experiments, we can observe the critical non-Hermitian skin effects by directly detecting the topological phase crossovers of the size-dependent in-gap boundary state. In ultracold atoms [74–78], the interface boundary between topologically trivial and nontrivial chains can be created by introducing a very large potential step (see details in Appendix D).

#### IV. CONCLUSION

We have shown theoretically that the NHSE can occur in a periodically driven ultracold atoms in the presence of the staggered atomic loss. The NHSE is characterized by the winding number, which is quite robust against the disorder. The underlying mechanism governing the periodic-drive-induced NHSE was provided by considering the Floquet-Magnus expansion in the high-frequency approximation. Moreover, we proposed observing the critical skin effect with the appearance of size-dependent topological in-gap modes by coupling two periodically driven chains with different driving phases. Our approach can be easily implemented in ultracold atoms based on Floquet engineering. Floquet engineering has emerged as a powerful experimental method for the realization of novel quantum systems in ultracold-atom systems. Our work paves the way for further studies of the NHSE and its interplay with many-body statistics and interactions in ultracold-atom systems.

#### ACKNOWLEDGMENTS

T.L. acknowledges support from the Introduced Innovative Team Project of Guangdong Pearl River Talents Program (Grant No. 2021ZT09Z109), the Fundamental Research Funds for the Central Universities (Grant No. 2023ZYGXZR020), National Natural Science Foundation of

China (Grant No. 12274142), and the Startup Grant of South China University of Technology (Grant No. 20210012).

#### APPENDIX A: REALIZATION OF THE FLOQUET HAMILTONIAN IN ULTRACOLD ATOMS

In this Appendix we provide some details to realize the dissipative Floquet Hamiltonian  $\mathcal{H}_p(t) = \mathcal{H}_0 + \mathcal{H}_d(t)$  in Eqs. (1) and (2), which consist of the periodically modulated staggered on-site potential and tilted potential and the staggered dissipation rates  $\lambda_1$  and  $\lambda_2 = \lambda_1 + \lambda$  at odd and even sites.

As shown in Fig. 8(a), in the experimental setting, the one-dimensional dynamical optical superlattice (in the  $x$  direction) in the presence of the periodically modulated staggered on-site potential can be created by superimposing a stationary lattice (i.e., the short lattice) with a period of  $\lambda_S$  and a dynamical interferometric lattice (i.e., the long lattice) with a period of  $\lambda_L = 2\lambda_S$  [79–81]. The phase of the dynamical interferometric lattice is periodically driven in time and controlled by a Michelson interferometer. The strong confinement in the  $y$  and  $z$  directions is provided by other optical lattices. The dynamical superlattice potential is written as

$$V_1(x, y, z, t) = -V_S(t) \cos^2(k_S x) - V_L(t) \cos^2[k_S x/2 - \varphi(t)], \quad (\text{A1})$$

where  $V_S$  and  $V_L$  are the depths of the short and long lattices controlled by the respective laser powers,  $k_S = 2\pi/\lambda_S$  is the wave vector, and  $\varphi(t)$  is the phase difference between the two lattices controlled by changing the optical path difference between the two interfering beams [79–81]. The ultracold atomic gases are loaded into this dynamically controlled optical superlattice and prepared in the first band. The band gaps between the first and the higher-level bands are fairly large at each well; we can focus on only the first band [79–81]. Then, in the tight-binding limit, we can achieve periodically modulated staggered on-site potential in the second term of the right-hand side of the Hamiltonian  $\mathcal{H}_d(t)$  in Eq. (2).

Further, in order to construct the periodically modulated tilted potential, we superimpose an additional drive consisting of a time-periodic modulation of the lattice position  $x$  with

the frequency  $\omega$ , as shown in Fig. 8(b). The time-periodic modulation of the lattice site has the form

$$V_2(x, y, z, t) = -V[x - A \cos(\omega t + \phi_c)], \quad (\text{A2})$$

where  $A$  is the modulation amplitude and  $\phi_c$  is phase. Such a tilted potential under periodic modulation (i.e., the time-dependent force) has been experimentally realized in ultracold-atom systems [62,82]. Then, in the tight-binding limit, we can achieve periodically modulated tilted potential in the first term of the right-hand side of the Hamiltonian  $\mathcal{H}_d(t)$  in Eq. (2).

Finally, when the atoms are prepared in the first-band state, the staggered dissipation rates  $\lambda_1$  and  $\lambda_2 = \lambda_1 + \lambda$  at odd and even sites in  $\mathcal{H}_0$  are realized via exciting the state in the first band at even sites to the higher-level state  $|e\rangle$ , where the additional dissipation  $\lambda$  is controlled by the intensity of the external optical beam [see Fig. 8(c)]. In order to selectively excite the atoms at even sites, we can utilize the ground-state hyperfine states in the combination of the Raman-assisted hopping between adjacent sites. To be specific, we consider ultracold atoms with two internal states, e.g., spin up and spin down. The spin-up states at the odd sites hop to spin-down states at the even sites using Raman-assisted hopping. Then the staggered dissipation can be realized by exciting all the spin-down states at the even sites to higher-level states. Note that the loss control using different internal states in the optical lattice of ultracold atoms has been experimentally reported [38,52,83,84].

### APPENDIX B: UNITARY TRANSFORMATION OF THE FLOQUET HAMILTONIAN

As shown in the main text, we construct the periodically driven Hamiltonian  $\mathcal{H}_p(t) = \mathcal{H}_0 + \mathcal{H}_d(t)$ , with

$$\mathcal{H}_0 = -J \sum_{j=1}^{L-1} (c_{j+1}^\dagger c_j + \text{H.c.}) - i\lambda \sum_{j=1}^{L/2} n_{2j}, \quad (\text{B1})$$

$$\mathcal{H}_d(t) = \sum_{j=1}^L F \left( \cos(\omega t + \phi) j + \sin(\omega t) \frac{3 + (-1)^j}{2} \right) n_j, \quad (\text{B2})$$

where, without loss of generality, we set  $\lambda_1 = 0$ . After performing a unitary transformation  $\mathcal{H}(t) = \mathcal{U} \mathcal{H}_p(t) \mathcal{U}^\dagger - i\mathcal{U} \partial_t \mathcal{U}^\dagger$ , with  $\mathcal{U}(t)$  being written as

$$\mathcal{U}(t) = \exp \left[ i \left( \frac{F}{\omega} \sin(\omega t + \phi) \sum_j^n j n_j - \frac{F}{\omega} \cos(\omega t) \sum_j^n \frac{3 + (-1)^j}{2} n_j \right) \right], \quad (\text{B3})$$

we achieve the periodically driven Hamiltonian as

$$\mathcal{H}(t) = \sum_{j=1}^{L/2} [(uc_{2j}^\dagger c_{2j-1} + \text{H.c.}) - i\lambda n_{2j}] - \sum_{j=1}^{L/2-1} (vc_{2j+1}^\dagger c_{2j} + \text{H.c.}), \quad (\text{B4})$$

where

$$u = -J e^{i\sqrt{2}\alpha \cos(\phi/2 + \pi/4) \sin(\omega t + \phi/2 - \pi/4)}, \quad (\text{B5})$$

$$v = -J e^{i\sqrt{2}\alpha \sin(\phi/2 + \pi/4) \cos(\omega t + \phi/2 - \pi/4)}, \quad (\text{B6})$$

with  $\alpha = \sqrt{2}F/\omega$ .

### APPENDIX C: EFFECTIVE HAMILTONIAN VIA FLOQUET-MAGNUS EXPANSION

In this Appendix we provide some details to obtain the time-independent effective Hamiltonian  $\mathcal{H}_{\text{eff}}$  by applying the Floquet-Magnus expansion [67–69] in the high-frequency approximation ( $\omega \gg J, F$ ). Up to the first-order approximation, the effective Hamiltonian is written as

$$\mathcal{H}_{\text{eff}} = \sum_{\mu=0,1} \mathcal{H}_{\text{eff}}^{(\mu)}, \quad (\text{C1})$$

where

$$\mathcal{H}_{\text{eff}}^{(0)} = \mathcal{H}_0, \quad \mathcal{H}_{\text{eff}}^{(1)} = \sum_{m \neq 0} \frac{[\mathcal{H}_{-m}, \mathcal{H}_m]}{2m\omega}, \quad (\text{C2})$$

with  $\mathcal{H}_m = T^{-1} \int_0^T \mathcal{H}(t) e^{im\omega t} dt$ .

We first derive the effective high-frequency Hamiltonian for the real-space model  $\mathcal{H}(t)$  in Eq. (3). For  $m \neq 0$  and  $\phi = 0, \pi$ ,  $\mathcal{H}_m$  reads

$$\mathcal{H}_m = \sum_j \left[ P_m \left( \frac{3\pi}{4} \right) c_{2j}^\dagger c_{2j-1} + P_m \left( -\frac{\pi}{4} \right) c_{2j-1}^\dagger c_{2j} \right] + \sum_j \left[ P_m \left( \frac{\pi}{4} \right) c_{2j+1}^\dagger c_{2j} + P_m \left( -\frac{3\pi}{4} \right) c_{2j}^\dagger c_{2j+1} \right], \quad (\text{C3})$$

where

$$P_m(\Phi) = -J i^{-m} J_{-m}(\alpha) e^{ims\Phi}, \quad (\text{C4})$$

with  $J_m(\alpha)$  the Bessel function of the first kind and  $s = 1$  ( $-1$ ) corresponding to  $\phi = 0$  ( $\pi$ ). According to Eqs. (C1)–(C3), we obtain the effective time-independent Hamiltonian  $\mathcal{H}_{\text{eff}}$  of  $\mathcal{H}(t)$  as

$$\mathcal{H}_{\text{eff}} = - \sum_j [J J_0(\alpha) c_{2j}^\dagger c_{2j-1} + J J_0(\alpha) c_{2j+1}^\dagger c_{2j} + \text{H.c.}] - \sum_{j=1} \left( i s \frac{2J^2 J_{-1}^2(\alpha)}{\omega} c_{2j+1}^\dagger c_{2j-1} + \text{H.c.} \right) + \sum_j \left( i s \frac{2J^2 J_{-1}^2(\alpha)}{\omega} c_{2j+2}^\dagger c_{2j} + \text{H.c.} \right) - i\lambda \sum_j c_{2j}^\dagger c_{2j}, \quad (\text{C5})$$

where only the term with  $m = 1$  is considered in the high-frequency limit in Eq. (C2).

We now derive the effective high-frequency Hamiltonian for the momentum-space Hamiltonian  $\mathcal{H}(k, t)$ . We rewrite

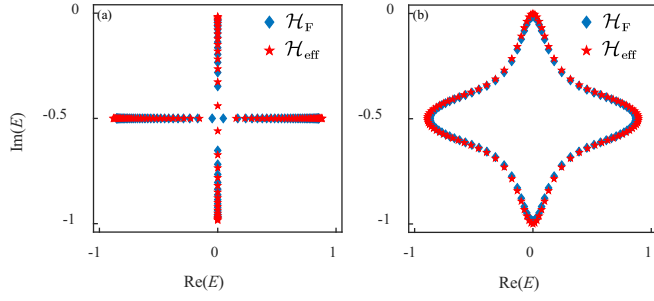


FIG. 9. Complex quasienergy spectrum  $E_n$  calculated using the Floquet Hamiltonian  $\mathcal{H}_F$  (blue diamonds) and effective Hamiltonian  $\mathcal{H}_{\text{eff}}$  (red stars) in the high-frequency limit under (a) OBCs and (b) PBCs. The parameters are  $\alpha = 1.5$ ,  $\omega = 3\pi$ ,  $\lambda/J = 1$ , and  $L = 100$ .

$\mathcal{H}(t)$  in Eq. (3) as

$$\mathcal{H}(t) = \sum_j [(uc_{j,B}^\dagger c_{j,A} + vc_{j+1,A}^\dagger c_{j,B} + \text{H.c.}) - i\lambda n_{j,B}]. \quad (\text{C6})$$

Then the momentum-space Hamiltonian  $\mathcal{H}(k, t)$  is written as

$$\mathcal{H}(k, t) = \sum_k [(u^* + ve^{-ik})c_{k,A}^\dagger c_{k,B} + \text{H.c.}] - i\lambda \sum_k c_{k,B}^\dagger c_{k,B}, \quad (\text{C7})$$

where  $A$  and  $B$  denote two sublattice sites in the unit cell due to the staggered loss. For  $m \neq 0$  and  $\phi = 0, \pi$ ,  $\mathcal{H}_m(k)$  reads

$$\mathcal{H}_m(k) = \sum_k [Q_{m,1}(k)c_{k,A}^\dagger c_{k,B} + Q_{m,2}(k)c_{k,B}^\dagger c_{k,A}], \quad (\text{C8})$$

where

$$Q_{m,1}(k) = -Ji^{-m}J_{-m}(\alpha)(e^{-ism(\pi/4)} + e^{ism(\pi/4)}e^{-ik}), \quad (\text{C9})$$

$$Q_{m,2}(k) = -Ji^{-m}J_{-m}(\alpha)(e^{ism(3\pi/4)} + e^{-ism(3\pi/4)}e^{ik}). \quad (\text{C10})$$

According to Eqs. (C1) and (C8), we obtain the effective time-independent Hamiltonian  $\mathcal{H}_{\text{eff}}(k)$  of  $\mathcal{H}(k, t)$  as

$$\begin{aligned} \mathcal{H}_{\text{eff}}(k) = & - \sum_k [JJ_0(\alpha)(1 + e^{-ik})c_{k,A}^\dagger c_{k,B} + \text{H.c.}] \\ & - s \frac{2J^2 J_{-1}^2(\alpha)}{\omega} \sum_k \sin(k)(c_{k,A}^\dagger c_{k,A} - c_{k,B}^\dagger c_{k,B}) \\ & - i\lambda \sum_k c_{k,B}^\dagger c_{k,B}, \end{aligned} \quad (\text{C11})$$

$$H_L(k, t) = \begin{pmatrix} 0 & -J_- - J_+ e^{-ik} & -\gamma & 0 \\ -J_-^* - J_+^* e^{ik} & -i\lambda & 0 & -\gamma \\ -\gamma & 0 & 0 & -J_+ - J_- e^{-ik} \\ 0 & -\gamma & -J_+^* - J_-^* e^{ik} & -i\lambda \end{pmatrix}. \quad (\text{D1})$$

The Floquet Hamiltonian  $H_L^F(k)$  of the ladder in momentum space is defined as  $U(T) = \mathcal{T} \exp[-i \int_0^T H_L(k, t') dt'] = e^{-iH_L^F(k)T}$ .

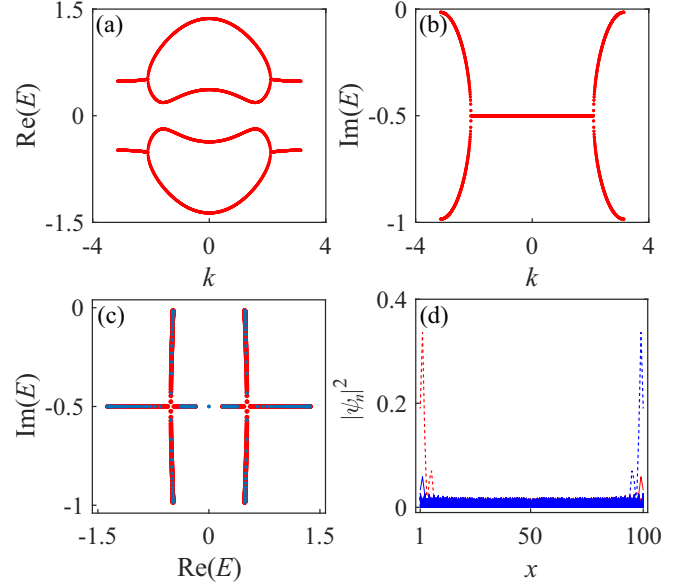


FIG. 10. (a) Real part and (b) imaginary part of the complex quasienergy spectrum of the Floquet Hamiltonian  $\mathcal{H}_L^F(k)$  of  $\mathcal{H}(k, t)$  in the momentum space. (c) Complex quasienergy spectrum  $E_n$  of the ladder under PBCs (red dots) and OBCs (blue dots). (d) Corresponding density distribution of the ladder under OBCs. The red and blue lines represent states in legs  $a$  and  $b$ , respectively. The dashed lines denote the topological in-gap boundary states. The parameters are  $\alpha = 1.5$ ,  $\omega = 3\pi$ ,  $\lambda/J = 1$ ,  $\gamma/J = 0.5$ , and  $L = 100$ .

with only the term with  $m = 1$  considered in the high-frequency limit in Eq. (C2).

In Fig. 9 we plot the OBC and PBC spectra, calculated using the Floquet Hamiltonian  $\mathcal{H}_F$  (blue diamonds) and effective Hamiltonian  $\mathcal{H}_{\text{eff}}$  (red stars). The effective Hamiltonian in the high-frequency limit shows a good approximation to the Floquet Hamiltonian.

#### APPENDIX D: TOPOLOGICAL PHASE OF THE PERIODICALLY DRIVEN LADDER

In this Appendix we give more details of the topological phases of the ladder system (see Fig. 6), which are protected by the energy gap and chiral symmetry. The momentum-space Hamiltonian of the ladder is written as  $\mathcal{H}_L(k, t) = \sum_k \Psi_k^\dagger H_L(k, t) \Psi_k$ , with  $\Psi_k = (a_{k,A}, a_{k,B}, b_{k,A}, b_{k,B})^T$ , where  $A$  and  $B$  denote sublattices along each leg, as shown by orange and blue circles in Fig. 6, and  $H_L(k, t)$  is

The Hamiltonian  $H_L(k, t)$  respects chiral symmetry  $SH_L(k, t)S^{-1} = -H_L^\dagger(k, -t)$ , where  $S = \sigma_y \tau_z$ , with Pauli matrices  $\sigma_{0,x,y,z}$  and  $\tau_{0,x,y,z}$  acting on the sublattices ( $A, B$ ) in



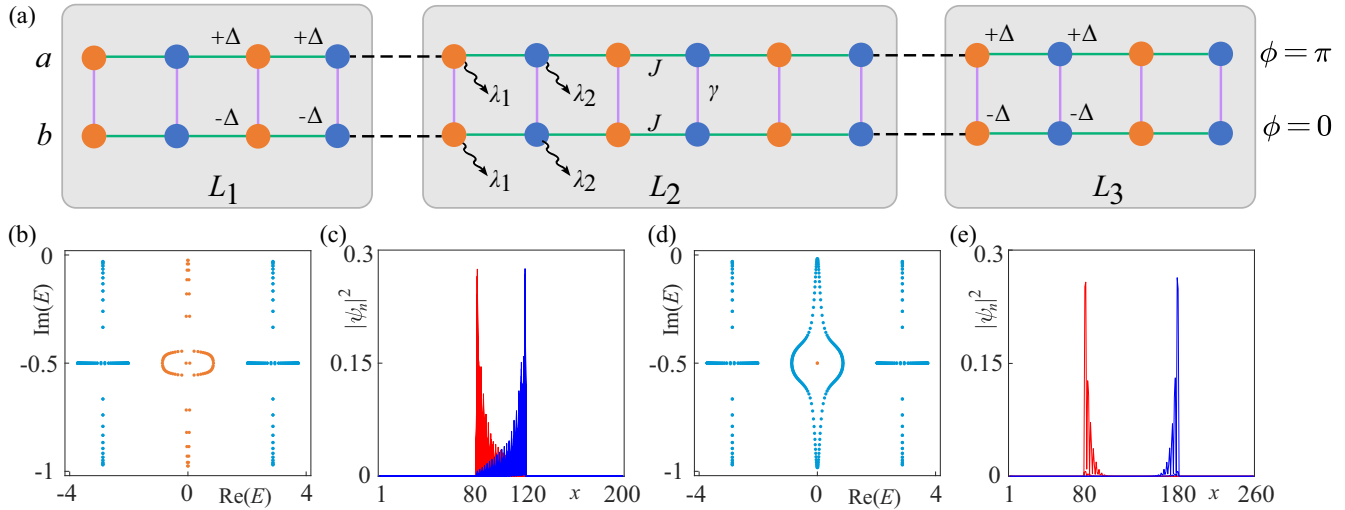


FIG. 11. (a) A middle ladder with size  $L_2$  is sandwiched by two ladders with lengths  $L_1$  and  $L_3$  in the presence of the very large on-site potential  $\Delta$  and  $-\Delta$  in chains  $a$  and  $b$ , respectively. (b) Complex-eigenenergy spectrum and (c) corresponding density distributions of states indicated by red dots in (b) for  $L_2 = 40$ . (d) Complex-eigenenergy spectrum and (e) density distributions of the topological in-gap states ( $E = -0.5i$ ) indicated by red dots in (d) for  $L_2 = 100$ . The parameters are  $\alpha = 1.5$ ,  $\omega = 3\pi$ ,  $\lambda/J = 1.0$ , and  $\gamma/J = 0.005$ .

each leg and the legs' ( $a, b$ ) degrees of freedom, receptively. As shown in Figs. 10(a) and 10(b), the Floquet Hamiltonian  $H_{\Gamma}^F(k)$  has a line gap. According to the topological classification of the Floquet non-Hermitian system [85], it supports a topological nontrivial phase. Figures 10(c) and 10(d) clearly show the degenerate in-gap boundary modes.

In experiments, we can observe the critical non-Hermitian skin effects by directly detecting the topological phase crossovers of the size-dependent in-gap boundary state. In ultracold atoms, the interface boundary between topologically trivial and nontrivial chains can be created by illuminating a selected area of the lattice with a large optical potential

[74–78]. As shown in Fig. 11(a), the middle ladder with the size  $L_2$  is sandwiched by two ladders with lengths  $L_1$  and  $L_3$  in the presence of the very large on-site potential  $\Delta$  and  $-\Delta$  in chains  $a$  and  $b$ . The left and right ladders are topologically trivial for large  $\Delta$  due to the broken chiral symmetry. We calculate the complex-eigenenergy spectrum and the corresponding density distributions for  $L_2 = 40$  [see Figs. 11(b) and 11(c)] and  $L_2 = 100$  [see Figs. 11(d) and 11(e)]. The results indicate that the eigenenergy spectrum and state density distribution of the middle ladder are largely separated from those of the left and right ladders and have the same features as the single ladder under OBCs (see Fig. 7) for large  $\Delta$ .

- [1] V. V. Konotop, J. Yang, and D. A. Zezyulin, Nonlinear waves in  $\mathcal{PT}$ -symmetric systems, *Rev. Mod. Phys.* **88**, 035002 (2016).
- [2] T. E. Lee, Anomalous edge state in a non-Hermitian lattice, *Phys. Rev. Lett.* **116**, 133903 (2016).
- [3] D. Leykam, K. Y. Bliokh, C. Huang, Y. D. Chong, and F. Nori, Edge modes, degeneracies, and topological numbers in non-Hermitian systems, *Phys. Rev. Lett.* **118**, 040401 (2017).
- [4] Y. Xu, S. T. Wang, and L. M. Duan, Weyl exceptional rings in a three-dimensional dissipative cold atomic gas, *Phys. Rev. Lett.* **118**, 045701 (2017).
- [5] Z. Gong, Y. Ashida, K. Kawabata, K. Takasan, S. Higashikawa, and M. Ueda, Topological phases of non-Hermitian systems, *Phys. Rev. X* **8**, 031079 (2018).
- [6] R. El-Ganainy, K. G. Makris, M. Khajavikhan, Z. H. Musslimani, S. Rotter, and D. N. Christodoulides, Non-Hermitian physics and  $\mathcal{PT}$  symmetry, *Nat. Phys.* **14**, 11 (2018).
- [7] S. Yao and Z. Wang, Edge states and topological invariants of non-Hermitian systems, *Phys. Rev. Lett.* **121**, 086803 (2018).
- [8] K. Zhang, Z. Yang, and C. Fang, Correspondence between winding numbers and skin modes in non-Hermitian systems, *Phys. Rev. Lett.* **125**, 126402 (2020).
- [9] K. Yokomizo and S. Murakami, Non-Bloch band theory of non-Hermitian systems, *Phys. Rev. Lett.* **123**, 066404 (2019).
- [10] S. Yao, F. Song, and Z. Wang, Non-Hermitian Chern bands, *Phys. Rev. Lett.* **121**, 136802 (2018).
- [11] F. K. Kunst, E. Edvardsson, J. C. Budich, and E. J. Bergholtz, Biorthogonal bulk-boundary correspondence in non-Hermitian systems, *Phys. Rev. Lett.* **121**, 026808 (2018).
- [12] T. Liu, Y.-R. Zhang, Q. Ai, Z. Gong, K. Kawabata, M. Ueda, and F. Nori, Second-order topological phases in non-Hermitian systems, *Phys. Rev. Lett.* **122**, 076801 (2019).
- [13] L. Zhou and J. Gong, Non-Hermitian Floquet topological phases with arbitrarily many real-quasienergy edge states, *Phys. Rev. B* **98**, 205417 (2018).
- [14] L. Zhou, Dynamical characterization of non-Hermitian Floquet topological phases in one dimension, *Phys. Rev. B* **100**, 184314 (2019).
- [15] A. Banerjee and A. Narayan, Controlling exceptional points with light, *Phys. Rev. B* **102**, 205423 (2020).
- [16] F. Song, S. Yao, and Z. Wang, Non-Hermitian skin effect and chiral damping in open quantum systems, *Phys. Rev. Lett.* **123**, 170401 (2019).

- [17] J. Y. Lee, J. Ahn, H. Zhou, and A. Vishwanath, Topological correspondence between Hermitian and non-Hermitian systems: Anomalous dynamics, *Phys. Rev. Lett.* **123**, 206404 (2019).
- [18] K. Kawabata, T. Bessho, and M. Sato, Classification of exceptional points and non-Hermitian topological semimetals, *Phys. Rev. Lett.* **123**, 066405 (2019).
- [19] C. H. Lee and R. Thomale, Anatomy of skin modes and topology in non-Hermitian systems, *Phys. Rev. B* **99**, 201103(R) (2019).
- [20] Z. Y. Ge, Y. R. Zhang, T. Liu, S. W. Li, H. Fan, and F. Nori, Topological band theory for non-Hermitian systems from the Dirac equation, *Phys. Rev. B* **100**, 054105 (2019).
- [21] H. Zhou and J. Y. Lee, Periodic table for topological bands with non-Hermitian symmetries, *Phys. Rev. B* **99**, 235112 (2019).
- [22] H. Zhao, X. Qiao, T. Wu, B. Midya, S. Longhi, and L. Feng, Non-Hermitian topological light steering, *Science* **365**, 1163 (2019).
- [23] K. Kawabata, K. Shiozaki, M. Ueda, and M. Sato, Symmetry and topology in non-Hermitian physics, *Phys. Rev. X* **9**, 041015 (2019).
- [24] D. S. Borgnia, A. J. Kruchkov, and R.-J. Slager, Non-Hermitian boundary modes and topology, *Phys. Rev. Lett.* **124**, 056802 (2020).
- [25] T. Liu, J. J. He, T. Yoshida, Z.-L. Xiang, and F. Nori, Non-Hermitian topological Mott insulators in one-dimensional fermionic superlattices, *Phys. Rev. B* **102**, 235151 (2020).
- [26] L. Li, C. H. Lee, S. Mu, and J. Gong, Critical non-Hermitian skin effect, *Nat. Commun.* **11**, 5491 (2020).
- [27] K. Yokomizo and S. Murakami, Scaling rule for the critical non-Hermitian skin effect, *Phys. Rev. B* **104**, 165117 (2021).
- [28] Y. Ashida, Z. Gong, and M. Ueda, Non-Hermitian physics, *Adv. Phys.* **69**, 249 (2020).
- [29] K. Kawabata, M. Sato, and K. Shiozaki, Higher-order non-Hermitian skin effect, *Phys. Rev. B* **102**, 205118 (2020).
- [30] N. Okuma, K. Kawabata, K. Shiozaki, and M. Sato, Topological origin of non-Hermitian skin effects, *Phys. Rev. Lett.* **124**, 086801 (2020).
- [31] Y. Yi and Z. Yang, Non-Hermitian skin modes induced by on-site dissipations and chiral tunneling effect, *Phys. Rev. Lett.* **125**, 186802 (2020).
- [32] T. Liu, J. J. He, Z. Yang, and F. Nori, Higher-order Weyl-exceptional-ring semimetals, *Phys. Rev. Lett.* **127**, 196801 (2021).
- [33] L. Li, C. H. Lee, and J. Gong, Impurity induced scale-free localization, *Commun. Phys.* **4**, 42 (2021).
- [34] E. J. Bergholtz, J. C. Budich, and F. K. Kunst, Exceptional topology of non-Hermitian systems, *Rev. Mod. Phys.* **93**, 015005 (2021).
- [35] Y. Li, C. Liang, C. Wang, C. Lu, and Y.-C. Liu, Gain-loss-induced hybrid skin-topological effect, *Phys. Rev. Lett.* **128**, 223903 (2022).
- [36] K. Zhang, Z. Yang, and C. Fang, Universal non-Hermitian skin effect in two and higher dimensions, *Nat. Commun.* **13**, 2496 (2022).
- [37] K. Li and Y. Xu, Non-Hermitian absorption spectroscopy, *Phys. Rev. Lett.* **129**, 093001 (2022).
- [38] Z. Ren, D. Liu, E. Zhao, C. He, K. K. Pak, J. Li, and G.-B. Jo, Chiral control of quantum states in non-Hermitian spin-orbit-coupled fermions, *Nat. Phys.* **18**, 385 (2022).
- [39] K. Kawabata, T. Numasawa, and S. Ryu, Entanglement phase transition induced by the non-Hermitian skin effect, *Phys. Rev. X* **13**, 021007 (2023).
- [40] K. Zhang, C. Fang, and Z. Yang, Dynamical degeneracy splitting and directional invisibility in non-Hermitian systems, *Phys. Rev. Lett.* **131**, 036402 (2023).
- [41] C.-A. Li, B. Trauzettel, T. Neupert, and S.-B. Zhang, Enhancement of second-order non-Hermitian skin effect by magnetic fields, *Phys. Rev. Lett.* **131**, 116601 (2023).
- [42] X. Li, J. Liu, and T. Liu, Localization-delocalization transitions in non-Hermitian Aharonov-Bohm cages, *Front. Phys.* **19**, 33211 (2024).
- [43] N. Okuma and M. Sato, Non-Hermitian topological phenomena: A review, *Annu. Rev. Condens. Matter Phys.* **14**, 83 (2023).
- [44] K. Kawabata and S. Ryu, Nonunitary scaling theory of non-Hermitian localization, *Phys. Rev. Lett.* **126**, 166801 (2021).
- [45] R. Lin, T. Tai, L. Li, and C. H. Lee, Topological non-Hermitian skin effect, *Front. Phys.* **18**, 53605 (2023).
- [46] S. Weidemann, M. Kremer, T. Helbig, T. Hofmann, A. Stegmaier, M. Greiter, R. Thomale, and A. Szameit, Topological funneling of light, *Science* **368**, 311 (2020).
- [47] K. Wang, A. Dutt, K. Y. Yang, C. C. Wojcik, J. Vučković, and S. Fan, Generating arbitrary topological windings of a non-Hermitian band, *Science* **371**, 1240 (2021).
- [48] Q. Zhou, J. Wu, Z. Pu, J. Lu, X. Huang, W. Deng, M. Ke, and Z. Liu, Observation of geometry-dependent skin effect in non-Hermitian phononic crystals with exceptional points, *Nat. Commun.* **14**, 4569 (2023).
- [49] T. Helbig, T. Hofmann, S. Imhof, M. Abdelghany, T. Kiessling, L. W. Molenkamp, C. H. Lee, A. Szameit, M. Greiter, and R. Thomale, Generalized bulk-boundary correspondence in non-Hermitian topoelectrical circuits, *Nat. Phys.* **16**, 747 (2020).
- [50] D. Zou, T. Chen, W. He, J. Bao, C. H. Lee, H. Sun, and X. Zhang, Observation of hybrid higher-order skin-topological effect in non-Hermitian topoelectrical circuits, *Nat. Commun.* **12**, 7201 (2021).
- [51] L. Li, C. H. Lee, and J. Gong, Topological switch for non-Hermitian skin effect in cold-atom systems with loss, *Phys. Rev. Lett.* **124**, 250402 (2020).
- [52] Q. Liang, D. Xie, Z. Dong, H. Li, H. Li, B. Gadway, W. Yi, and B. Yan, Dynamic signatures of non-Hermitian skin effect and topology in ultracold atoms, *Phys. Rev. Lett.* **129**, 070401 (2022).
- [53] S. Giorgini, L. P. Pitaevskii, and S. Stringari, Theory of ultracold atomic Fermi gases, *Rev. Mod. Phys.* **80**, 1215 (2008).
- [54] D.-W. Zhang, Y.-Q. Zhu, Y. X. Zhao, H. Yan, and S.-L. Zhu, Topological quantum matter with cold atoms, *Adv. Phys.* **67**, 253 (2018).
- [55] N. R. Cooper, J. Dalibard, and I. B. Spielman, Topological bands for ultracold atoms, *Rev. Mod. Phys.* **91**, 015005 (2019).
- [56] F. Schäfer, T. Fukuhara, S. Sugawa, Y. Takasu, and Y. Takahashi, Tools for quantum simulation with ultracold atoms in optical lattices, *Nat. Rev. Phys.* **2**, 411 (2020).
- [57] L. Zhou, H. Li, W. Yi, and X. Cui, Engineering non-Hermitian skin effect with band topology in ultracold gases, *Commun. Phys.* **5**, 252 (2022).
- [58] S. Guo, C. Dong, F. Zhang, J. Hu, and Z. Yang, Theoretical prediction of a non-Hermitian skin effect in ultracold-atom systems, *Phys. Rev. A* **106**, L061302 (2022).

- [59] N. Goldman and J. Dalibard, Periodically driven quantum systems: Effective Hamiltonians and engineered gauge fields, *Phys. Rev. X* **4**, 031027 (2014).
- [60] N. Goldman, J. C. Budich, and P. Zoller, Topological quantum matter with ultracold gases in optical lattices, *Nat. Phys.* **12**, 639 (2016).
- [61] A. Eckardt, *Colloquium*: Atomic quantum gases in periodically driven optical lattices, *Rev. Mod. Phys.* **89**, 011004 (2017).
- [62] F. Görg, K. Sandholzer, J. Minguzzi, R. Desbuquois, M. Messer, and T. Esslinger, Realization of density-dependent Peierls phases to engineer quantized gauge fields coupled to ultracold matter, *Nat. Phys.* **15**, 1161 (2019).
- [63] C. Weitenberg and J. Simonet, Tailoring quantum gases by Floquet engineering, *Nat. Phys.* **17**, 1342 (2021).
- [64] Y. Li, C. Lu, S. Zhang, and Y.-C. Liu, Loss-induced Floquet non-Hermitian skin effect, *Phys. Rev. B* **108**, L220301 (2023).
- [65] C. Shu, K. Zhang, and K. Sun, Loss-induced universal one-way transport in periodically driven systems, *Phys. Rev. B* **109**, 184302 (2024).
- [66] M. S. Rudner and N. H. Lindner, Band structure engineering and non-equilibrium dynamics in Floquet topological insulators, *Nat. Rev. Phys.* **2**, 229 (2020).
- [67] M. Bukov, L. D'Alessio, and A. Polkovnikov, Universal high-frequency behavior of periodically driven systems: From dynamical stabilization to Floquet engineering, *Adv. Phys.* **64**, 139 (2015).
- [68] A. Eckardt and E. Anisimovas, High-frequency approximation for periodically driven quantum systems from a Floquet-space perspective, *New J. Phys.* **17**, 093039 (2015).
- [69] T. Mikami, S. Kitamura, K. Yasuda, N. Tsuji, T. Oka, and H. Aoki, Brillouin-Wigner theory for high-frequency expansion in periodically driven systems: Application to Floquet topological insulators, *Phys. Rev. B* **93**, 144307 (2016).
- [70] W. Zhu and J. Gong, Hybrid skin-topological modes without asymmetric couplings, *Phys. Rev. B* **106**, 035425 (2022).
- [71] H. Cai, J. Liu, J. Wu, Y. He, S.-Y. Zhu, J.-X. Zhang, and D.-W. Wang, Experimental observation of momentum-space chiral edge currents in room-temperature atoms, *Phys. Rev. Lett.* **122**, 023601 (2019).
- [72] S. M. Rafi-Ul-Islam, Z. B. Siu, H. Sahin, C. H. Lee, and M. B. A. Jalil, Critical hybridization of skin modes in coupled non-Hermitian chains, *Phys. Rev. Res.* **4**, 013243 (2022).
- [73] F. Qin, Y. Ma, R. Shen, and C. H. Lee, Universal competitive spectral scaling from the critical non-Hermitian skin effect, *Phys. Rev. B* **107**, 155430 (2023).
- [74] A. L. Gaunt, T. F. Schmidutz, I. Gotlibovych, R. P. Smith, and Z. Hadzibabic, Bose-Einstein condensation of atoms in a uniform potential, *Phys. Rev. Lett.* **110**, 200406 (2013).
- [75] N. Goldman, J. Dalibard, A. Dauphin, F. Gerbier, M. Lewenstein, P. Zoller, and I. B. Spielman, Direct imaging of topological edge states in cold-atom systems, *Proc. Natl. Acad. Sci. USA* **110**, 6736 (2013).
- [76] L. Chomaz, L. Corman, T. Bienaimé, R. Desbuquois, C. Weitenberg, S. Nascimbène, J. Beugnon, and J. Dalibard, Emergence of coherence via transverse condensation in a uniform quasi-two-dimensional Bose gas, *Nat. Commun.* **6**, 6162 (2015).
- [77] K. Hueck, N. Luick, L. Sobirey, J. Siegl, T. Lompe, and H. Moritz, Two-dimensional homogeneous Fermi gases, *Phys. Rev. Lett.* **120**, 060402 (2018).
- [78] C. Braun, R. Saint-Jalm, A. Hesse, J. Arceri, I. Bloch, and M. Aidelsburger, Real-space detection and manipulation of topological edge modes with ultracold atoms, *Nat. Phys.* (2024), doi: 10.1038/s41567-024-02506-z.
- [79] M. Lohse, C. Schweizer, O. Zilberberg, M. Aidelsburger, and I. Bloch, A Thouless quantum pump with ultracold bosonic atoms in an optical superlattice, *Nat. Phys.* **12**, 350 (2016).
- [80] S. Nakajima, T. Tomita, S. Taie, T. Ichinose, H. Ozawa, L. Wang, M. Troyer, and Y. Takahashi, Topological Thouless pumping of ultracold fermions, *Nat. Phys.* **12**, 296 (2016).
- [81] S. Nakajima, N. Takei, K. Sakuma, Y. Kuno, P. Marra, and Y. Takahashi, Competition and interplay between topology and quasi-periodic disorder in Thouless pumping of ultracold atoms, *Nat. Phys.* **17**, 844 (2021).
- [82] R. Desbuquois, M. Messer, F. Görg, K. Sandholzer, G. Jotzu, and T. Esslinger, Controlling the Floquet state population and observing micromotion in a periodically driven two-body quantum system, *Phys. Rev. A* **96**, 053602 (2017).
- [83] J. Li, A. K. Harter, J. Liu, L. de Melo, Y. N. Joglekar, and L. Luo, Observation of parity-time symmetry breaking transitions in a dissipative Floquet system of ultracold atoms, *Nat. Commun.* **10**, 855 (2019).
- [84] E. Zhao, Z. Wang, C. He, T. F. J. Poon, K. K. Pak, Y.-J. Liu, P. Ren, X.-J. Liu, and G.-B. Jo, Two-dimensional non-Hermitian skin effect in an ultracold Fermi gas, [arXiv:2311.07931](https://arxiv.org/abs/2311.07931).
- [85] C.-H. Liu, H. Hu, and S. Chen, Symmetry and topological classification of Floquet non-Hermitian systems, *Phys. Rev. B* **105**, 214305 (2022).